

# Quantifying residual orientation and thermal stress contributions to birefringence in the material extrusion of polylactide<sup>\*</sup>

Anthony P. Kotula<sup>a,\*</sup>, Benjamin E. Dolata<sup>a</sup>, Yoontae Kim<sup>a,b,c</sup>, Sara V. Orski<sup>a</sup>, Jonathan E. Seppala<sup>a</sup>

<sup>a</sup>Material Measurement Laboratory, National Institute of Standards and Technology, Gaithersburg, MD, 20899, USA

<sup>b</sup>Department of Biochemistry and Molecular & Cellular Biology, Georgetown University, Washington, DC, 20057, USA

<sup>c</sup>Center for Biological and Biomedical Engineering, Georgetown University, Washington, DC, 20057, USA

---

## Abstract

Material extrusion is a common additive manufacturing process that subjects polymers to non-steady deformation and thermal processing to build a customized part. The mechanical properties of these parts are often worse than those of injection-molded specimens due to failures at or near the weld zone between extrudate layers. Chain orientation is often cited as a contribution to mechanical weakness at the weld, and it is therefore of critical importance to develop strategies to quantify the magnitude and location of residual chain orientation as a function of printing conditions. Here we use birefringence imaging to characterize the spatial variation in residual stress and residual chain orientation in a glassy polylactide. A combination of retardance measurements and sample thickness measurements provide a measure of birefringence as a function of position. As-printed samples show a nearly uniform birefringence background of approximately  $7 \times 10^{-5}$  and higher birefringence near the weld region at lower nozzle temperatures and faster printing speeds. We propose two origins to the birefringence: one due to residual chain orientation, and the other due to residual stresses that occur when the sample cools non-uniformly on the build plate. Annealing the sample at 65 °C (slightly above the glass transition temperature) allows us to relax the residual stress without removing the orientation-based birefringence or crystallizing the sample. The residual orientation shows a strong power-law dependence on the Weissenberg number based on the characteristic timescales for flow in the nozzle and polymer chain reptation.

*Keywords:* material extrusion, chain orientation, residual stress, birefringence

---

## 1. Introduction

Material extrusion is an additive manufacturing process with applications ranging from aerospace, biomaterials, and 4D materials to desktop printing hobbyists.[1–3] Despite its ease of use, the material extrusion process is governed by rich polymer physics: molten polymers are extruded onto previously deposited extrudate layers, where the extrudate then rapidly cools as

---

<sup>\*</sup>Official contribution of the National Institute of Standards and Technology; not subject to copyright in the United States.

<sup>\*</sup>Corresponding author

Email address: anthony.kotula@nist.gov (Anthony P. Kotula)

Preprint submitted to Additive Manufacturing

January 9, 2025

6 polymer chains interdiffuse to form a weld. Each extrudate layer is subjected to fast, nonuniform  
7 deformation rates in the extrusion-deposition process. As a result, the printed part is comprised  
8 of many highly-deformed layers. This is a stark contrast to more conventional polymer process-  
9 ing technologies like injection molding, where a highly-deformed skin layer near the part surface  
10 comprises a small fraction of the overall part volume.[4] Each printed layer is also experiences  
11 a complex temperature history as heat from the deposited extrudate conducts through the sam-  
12 ple.[5, 6] The mechanical and optical properties of the final part therefore reflect the process  
13 history of each layer and the welding between them.

14 The extrusion and deposition process common in material extrusion can impart significant  
15 microscale anisotropy that can vary across the dimensions of the printed part. As the polymer  
16 melt flows through the nozzle and is deposited during the material extrusion process, the shear  
17 and extensional deformation gradients at the macroscale result in changes to the average orien-  
18 tation or stretching of the entangled chains from their equilibrium coiled state. These molecular-  
19 scale anisotropies become "trapped" in the part due to their inability to relax once the polymer  
20 solidifies. Both shear and extension can orient and stretch chains, but chains are much more sen-  
21 sitive to extensional deformation.[7, 8] This molecular-scale dependence on macroscale flows  
22 has been exploited in material extrusion to generate orientation-dependent mechanical properties  
23 in fiber-reinforced epoxy inks [9] and liquid-crystal polymers.[10, 11] Molecular anisotropy also  
24 changes the optical properties of the material. Recent work has shown that processing condi-  
25 tions can be used to encode information in parts via position-dependent birefringence.[12] This  
26 residual orientation is not constant throughout the material but is expected to be greater near  
27 the weld region between extrudate layers due to the material deformation during extrusion and  
28 deposition.[7]

29 Near-weld orientation will dramatically affect the mechanical properties of the final part.  
30 Increased chain orientation near the weld region weakens the weld strength in amorphous poly-  
31 mers.[13–15] Semicrystalline polymers show enhanced nucleation density near the weld due to  
32 increased chain deformation imparted from the extrusion-deposition process.[16] This enhanced  
33 crystallization has been shown to hinder weld formation.[17] It is therefore critical to character-  
34 ize the degree and location of oriented regions throughout the part.

35 Chain orientation has been measured in printed parts using polarized optical microscopy,[14]  
36 polarized infrared and Raman spectroscopy,[15, 18] and X-ray scattering,[19] which generally  
37 indicate a higher degree of orientation at the polymer-air interface and near polymer-polymer  
38 weld zones. However, these measurements were unable to assess the spatial variation in residual  
39 orientation across each extrudate layer. Birefringence imaging is a well-established technique for  
40 generating spatial maps of residual stress and chain orientation in transparent injection-molded  
41 polymers,[20] but this technique has not been applied to characterize parts printed by material  
42 extrusion. In birefringence imaging, circularly polarized light is directed through a birefrin-  
43 gent sample, and the resulting change in ellipticity of the transmitted light is measured by a  
44 polarization-sensitive detector to generate an image of the sample's retardance (also called the  
45 optical path difference) and the principal axis of orientation. This technique is generally used on  
46 samples with flat surfaces for transmission of the polarized light, but the surface of a printed part  
47 consists of many highly curved extrudate layers. This high curvature, which is primarily near  
48 the weld region between two extrudate layers, causes refraction at the air-polymer interface and  
49 makes spatial mapping of optical properties across extrudate layers in air impossible. Since this  
50 refraction is caused by differences between the refractive index of air (approximately 1) and the  
51 polymer (generally in the range of 1.3 to 1.7),[21] a straightforward solution is to immerse the  
52 sample in a fluid with a refractive index that is approximately equal to the refractive index of the

53 polymer.

54 Additionally, prior efforts to quantify residual orientation via optical methods neglect the possi-  
55 bility of other contributions to birefringence. In addition to residual chain orientation, residual  
56 stresses are known to occur in amorphous polymers that experience a spatial temperature gra-  
57 dient when cooled below the glass transition temperature.[22] In injection-molded parts, for  
58 example, the center of a molded part cools more slowly than the polymer near the wall of the  
59 mold, which results in residual stresses that vary from the polymer-mold surface to the core of  
60 the injection-molded part.[23] These thermal stresses are known to affect the mechanical and  
61 fracture properties of glassy polymers,[24, 25] and it is therefore critical to know whether these  
62 stresses occur in printed parts.

63 In this work, we use birefringence imaging in a refractive index matching fluid to deter-  
64 mine position-dependent residual orientation in extrudate layers. Imaging a sample printed from  
65 polylactide (PLA) in a glycerol-water mixture that closely matches the refractive index of the  
66 polymer allows us to quantify the retardance near the weld region. By combining these measure-  
67 ments with measurements of the sample thickness we can directly measure birefringence as a  
68 function of position across each extrudate layer. We identify different origins of birefringence in  
69 printed parts and demonstrate a simple annealing process that allows us to isolate birefringence  
70 due to trapped chain orientation. Lastly, we demonstrate a strong scaling relationship between  
71 the residual orientation near the weld region and the processing conditions in the printer nozzle.

## 72 2. Materials and Methods

### 73 2.1. Materials

74 “Natural” color polylactide filament (Premium PLA) was purchased from AirWolf 3D.<sup>1</sup> The  
75 filament diameter was  $(2.85 \pm 0.05)$  mm. Sections of filament were dried overnight at  $60^\circ\text{C}$  under  
76 vacuum prior to measurements or printing. Gel permeation chromatography measurements were  
77 performed on samples dissolved in tetrahydrofuran and measured against polystyrene standards  
78 (Agilent Technologies, EasiCal PS-2, linear calibration from 10 narrow dispersity PS standards  
79 of nominal  $M_p$  between 580 g/mol to 400,000 g/mol) to determine the molar mass averages and  
80 molar mass distribution. The mass average molar mass was  $(103.3 \pm 0.4)$  kg/mol, and the dis-  
81 persity is  $1.64 \pm 0.05$  with the reported standard deviation resulting from 3 injections. Distilled,  
82 deionized water was produced from a Milli-Q filtration system to a resistivity of  $18.2\text{ M}\Omega \cdot \text{cm}$   
83 and mixed with glycerol (anhydrous, J.T. Baker) to produce a solution of approximate mass frac-  
84 tion of 94 %. Refractive index matching between the glycerol solution and PLA was determined  
85 visually by immersing a section of filament in solution and observing minimal refraction through  
86 the filament.

### 87 2.2. Rheology

88 Sections of filament were loaded between 8 mm parallel plates in a stress-controlled rheome-  
89 ter (MARS III, Thermo Fisher) at  $200^\circ\text{C}$ . The upper plate was lowered to a gap height of 1 mm  
90 and the sample was trimmed prior to rheological measurements. Small-amplitude oscillatory

---

<sup>1</sup>Certain commercial equipment, instruments, software, or materials are identified in this paper in order to specify the experimental procedure adequately. Such identification is not intended to imply recommendation or endorsement by the National Institute of Standards and Technology, nor is it intended to imply that the materials or equipment identified are necessarily the best available for the purpose.

91 shear measurements were performed by setting the desired temperature, waiting for 5 min, and  
92 then perform oscillatory measurements with a fixed strain amplitude of 0.05 over a frequency  
93 range of 1 rad/s to 100 rad/s. Measurements were assessed using a van Gurp-Palmen plot [26]  
94 of the phase angle  $\delta$  versus the magnitude of the complex modulus  $G^*$  to ensure that the samples  
95 were thermorheologically simple over the temperature range used, 140 °C to 220 °C.

### 96 2.3. *Printing*

97 Samples were printed using an Axiom Dual Drive Direct 3D Printer (AirWolf 3D) with a  
98 nozzle diameter of 0.5 mm using an expanded range of printing conditions from prior work.[16]  
99 The printer was modified with circular cutouts on each side to allow infrared and visible light  
100 imaging of the printing process. The nozzle temperature range was 175 °C to 250 °C and the  
101 nominal print speeds (x,y-translation) were 10 mm/s, 30 mm/s, and 100 mm/s. The bed temper-  
102 ature was 50.5 °C at the print position, the cooling fan was disabled, and the room temperature  
103 was approximately 22 °C. The samples are printed with the following input dimensions: 100 mm  
104 long (x-axis), 4.5 mm tall (z-axis, 15 layers at 0.3 mm), and 0.5 mm wide (y-axis, nozzle diam-  
105 eter). The sample was printed approximately 30 mm from the left edge of the build plate. To  
106 prevent sample detachment, 10 mm by 10 mm “adhesion feet” are added to the first layer and the  
107 first layer is over-extruded by 125 %. The print direction is always front to back with the nozzle  
108 returning out of the print plane, 40 mm from the left edge. All travel moves (no extrusion) are  
109 250 mm/s. A Perl script was used to generate GCODEs for each print. The relative extrusion  
110 rate was calculated assuming a 2.85 mm filament diameter and a 0.3 mm by 0.5 mm extrudate  
111 rectangular cross section.

### 112 2.4. *Optical characterization*

113 For all polarization measurements, samples are imaged in the x-z axis defined in subsection  
114 2.3. Polarized optical measurements were performed using either a polarized optical microscope  
115 (Olympus BX-51) or a polarization camera (Photron). Schematics of the optical trains for both  
116 instruments are shown in Figure 1. In the polarization optical microscope (Figure 1a), white light  
117 is polarized by a linear polarizer, then sent through a condenser to the sample which is immersed  
118 in the 94 % glycerol solution. The sample is imaged using a 5x objective (LMPLFLN, Olympus),  
119 and the collected light is sent through additional optical elements depending on the characteri-  
120 zation method. For polarized optical imaging, a linearly-polarized analyzer oriented 90° to the  
121 polarizer is used. For quantitative near-weld retardance measurements, a Berek compensator  
122 (U-CBE, Olympus) was inserted between the objective and the analyzer. The compensator plate  
123 was tilted until extinction was first observed, and then the retardance was calculated from the tilt  
124 angle and the known optical properties of the plate. For white light illumination, the retardance  
125 range of this compensator is 0 nm to 1638 nm.

126 The polarization camera setup (Figure 1b) consists of a monochromatic 525 nm light source  
127 (Solis, ThorLabs), followed by a linear polarizer and quarter wave plate to generate circularly-  
128 polarized light. The light transmitted through the sample (immersed in the index matching solu-  
129 tion) was collected using an apochromatic zoom lens (Leica Z16 APO) attached to the camera.  
130 The image sensor of the camera is bonded to a pixelated polarizer array organized such that each  
131 2 pixel by 2 pixel subarray collects light polarized in four directions: 0°, 45°, 90°, and 135°  
132 (Figure 1c). The four intensities are used to calculate the total intensity, retardance, principal  
133 azimuthal angle in each subarray from known relationships.[27] The image sensor consists of a  
134 512 by 512 grid of subarrays for quantitative retardance imaging in the retardance range of 0 nm  
135 to 131 nm.

136 The two-dimensional retardance images can be converted to a one-dimensional retardance  
 137 profile by averaging the retardance over a distance of  $100\ \mu\text{m}$  in the printing direction. The  
 138 retardance profile is then reported as the average value  $\pm$  one standard deviation.

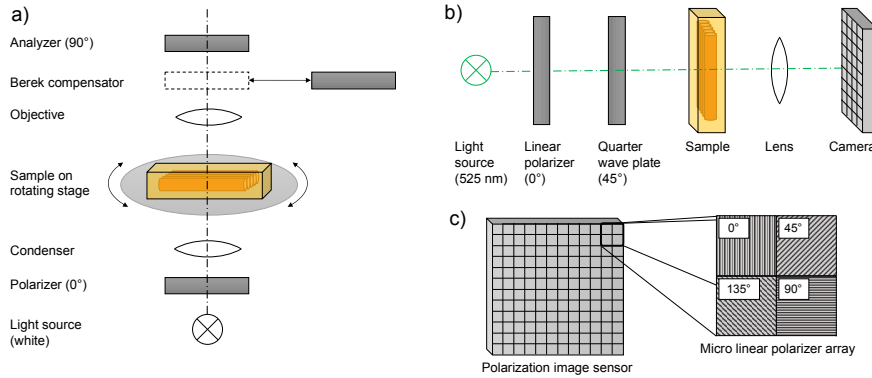


Figure 1: Schematic diagram of polarization instrumentation: a) Polarized optical microscope b) Birefringence imaging camera c) Diagram of polarization camera detector and micro linear polarizer array with four polarization states.

### 139 2.5. Thickness measurements and birefringence calculation

140 Measurements of the sample thickness  $w$  that the light passes through were performed using  
 141 optical microscopy. These measurements were performed using the polarized optical microscope  
 142 with the 5x objective described above. Sections of printed samples were cut using a precision  
 143 diamond saw and imaged with the polarizer and analyzer removed. Images were taken using  
 144 a 4 megapixel camera (ace Classic, Basler), and the distance calibration was performed using  
 145 a stage micrometer (Edmund Optics). The pixel-to-micron ratio was  $(0.46 \pm 0.02)$  pixel/ $\mu\text{m}$ .  
 146 These images were used to measure the sample thickness as a function of print height.

147 Once the retardance  $\rho$  and thickness  $w$  were determined, the birefringence  $\Delta n$  was calculated  
 148 via  $\rho = w\Delta n$ . To account for the difference in resolution between the retardance imaging setup  
 149 using the polarization camera (0.07 pixel/ $\mu\text{m}$ ) and the optical thickness measurements (0.46  
 150 pixel/ $\mu\text{m}$ ), the thickness profile was smoothed along the print height direction using a 6-point  
 151 moving average with a 6-point moving standard deviation. The thickness profile (average value  
 152  $\pm$  one standard deviation) was then downsampled via nearest neighbor interpolation to the re-  
 153 tardance profile to calculate the birefringence. The standard deviations in the retardance and  
 154 thickness were used to estimate the uncertainty in the calculated birefringence via propagation  
 155 of error.

### 156 2.6. Annealing

157 Sample annealing was performed by immersing approximately 4 mm sections of sample in  
 158 the 94 % glycerol solution in an optical shear cell (Linkam CSS450). The shear cell has heaters  
 159 above and below the sample, which allows for more uniform heating. Annealing conditions were  
 160 determined using a sample printed at  $250\ ^\circ\text{C}$  and a print speed of 10 mm/s. First, the sample was  
 161 immersed in the glycerol solution at room temperature in the shear cell. Next, the shear cell  
 162 was positioned on the microscope so that the sample was oriented approximately  $45^\circ$  to the  
 163 polarizer. Under these conditions the sample appeared bright under crossed polars. The sample

164 was then observed during a temperature ramp of 1 °C/min until the sample brightness decreased,  
 165 and the temperature where the brightness decrease occurred (65 °C) was chosen as the annealing  
 166 temperature. This temperature is approximately 5 °C above the glass transition temperature of  
 167 PLA.[28, 29]

168 Once the annealing temperature was identified, samples were annealed by loading the sam-  
 169 ples in the shear cell at room temperature, ramping up to the annealing temperature at a rate of  
 170 30 °C/min, then remaining at temperature for 3 min. After this time period, the heaters in the  
 171 shear cell were turned off. The sample was left in the shear cell until the reported temperature  
 172 from the shear cell fell below 35 °C, after which point the sample was removed from the shear  
 173 cell for characterization. Annealing using this technique resulted in samples that were optically  
 174 transparent.

175 Attempts to anneal batches of samples in a vacuum oven or in a water bath on a hot plate set  
 176 to a nominal temperature of 65 °C were unsuccessful, due to spatial temperature variations (hot  
 177 spots). Holding samples at higher temperatures (approximately 70 °C) for more than 10 minutes  
 178 resulted in opaque samples, indicating significant crystallization.

### 179 3. Results and Discussion

#### 180 3.1. Rheology

181 PLA melt rheology is shown in Figure 2. Small amplitude oscillatory measurements (shifted  
 182 using horizontal shift factors  $a_T$ ) form a master curve of the storage moduli  $G'$  and loss mod-  
 183 uli  $G''$  that can be fit using the Likhtman and McLeish reptation theory [30] using the RepTate  
 184 software.[31] The fit agrees relatively well with the data and provides information on the char-  
 185 acteristic relaxation timescales of the polymer. The primary timescale of interest is the reptation  
 186 time  $\tau_d$ , which governs the timescale for a polymer chain to diffuse out of its confining tube.  
 187 At 180 °C, the reptation time is  $\tau_d = (0.15 \pm 0.02)$  s. As the tube renewal timescale,  $\tau_d$  is a  
 188 characteristic relaxation time associate with the rate of stress relaxation.[32] Since the stress ten-  
 189 sor  $\sigma$  is linearly proportional to the refractive index tensor of the material  $\mathbf{n}$  via the stress-optic  
 190 rule,  $\mathbf{n} = C_{OR}\sigma$ ,[33] birefringence effects should be sensitive to this characteristic time. The  
 191 linear stress-optic rule for polymer melts holds over a wide range of strain rates, and well into  
 192 the region of non-Newtonian rheological properties.[34]

193 The Likhtman-McLeish fit also provides a measure of the Rouse timescale  $\tau_R$ , which is the  
 194 characteristic timescale for chain stretch relaxation. At 180 °C, the Rouse time is  $\tau_R = (4.2 \pm$   
 195  $0.6) \times 10^{-3}$  s, approximately 40 times faster than the reptation timescale.

196 Both reptation and stretch relaxation rates are slowed at lower temperatures. The relative  
 197 change in a relaxation timescale as a function of temperature is equal to the horizontal shift fac-  
 198 tors  $a_T$  used to generate the master curve. These shift factors increase with decreasing tempera-  
 199 ture  $T$ , as shown in the inset of Figure 2b, and are well-described by the Williams-Landell-Ferry  
 200 (WLF) equation[35]

$$\log a_T = \frac{-C_1 (T - T_0)}{C_2 + (T - T_0)}, \quad (1)$$

201 Here  $T_0$  is a reference temperature, and  $C_1$  and  $C_2$  are fit coefficients. At a reference temperature  
 202 of 180 °C, the shift factors are well-described by  $C_1 = 3.2 \pm 0.2$  and  $C_2 = (175.2 \pm 10.4)$  °C.

203 The steady shear properties of the polymer melt are also important for understanding the  
 204 effects of capillary flow in the printer nozzle during the material extrusion process. The steady

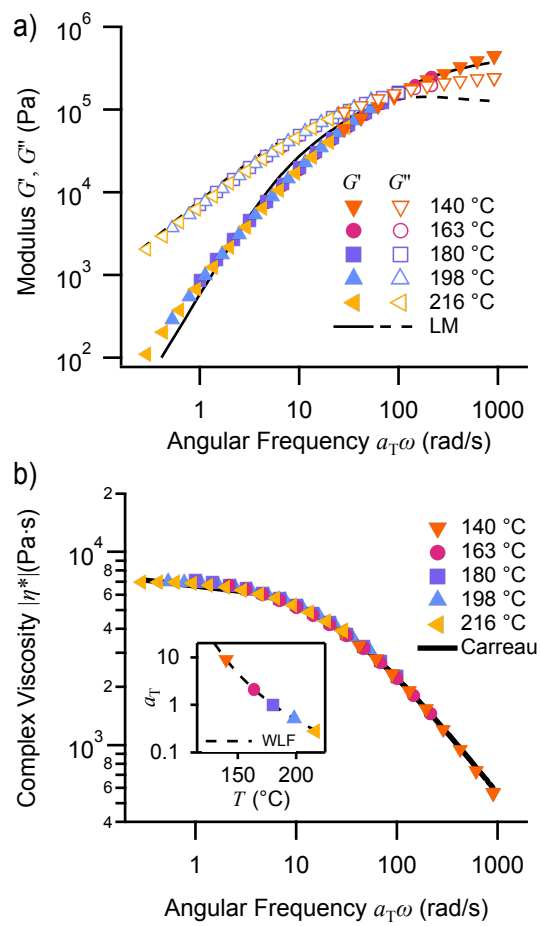


Figure 2: Linear rheology measurements of PLA. a) Small-amplitude oscillatory rheology master curve of the polylactide melt with the Likhtman-McLeish (“LM”) model fit b) Complex viscosity master curve with the Carreau-Yasuda (“Carreau”) fit. The inset plot shows the shift factors  $a_T$  as a function of temperature with the WLF fit.

205 shear viscosity  $\eta$  as a function of shear rate  $\dot{\gamma}$  can be estimated from the magnitude of complex  
 206 viscosity shown in Figure 2b using the Cox-Merz rule,  $|\eta^*(\omega)| = \eta(\dot{\gamma})_{\dot{\gamma}=\omega}$ . [36] The viscosity  
 207 exhibits a plateau at lower shear rates and significant shear thinning at higher shear rates, which  
 208 can be fit to the Carreau-Yasuda model. [37]

$$\frac{\eta - \eta_\infty}{\eta_0 - \eta_\infty} = [1 + (\lambda\dot{\gamma})^a]^{(n-1)/a} \quad (2)$$

209 Equation 2 has five fitting parameters corresponding to the zero shear viscosity  $\eta_0$ , a high shear  
 210 rate plateau viscosity  $\eta_\infty$ , a time constant  $\lambda$ , the power law index  $n$ , and a parameter  $a$  describing  
 211 the transition between the low shear rate plateau and the shear thinning region. At fast shear rates  
 212 ( $\lambda\dot{\gamma} \gg 1$ ), the viscosity follows a simple power law scaling  $\eta \sim \dot{\gamma}^{n-1}$ . For simplicity in fitting,  
 213 we set  $\eta_\infty = 0 \text{ Pa} \cdot \text{s}$  and determine the remaining four parameters, which are shown in Table  
 214 1. The parameters were determined based on a nonlinear curve fit of eq 2 using a Levenberg-  
 215 Marquardt algorithm, and the values are reported  $\pm$  one standard deviation. The shear thinning  
 216 exponent  $n$  is a critical parameter for estimating the flow profile in the printer nozzle.

Table 1: Fit parameters for Carreau-Yasuda viscosity model at the reference temperature 180 °C

Parameter	Value	Units
$\eta_0$	$7310 \pm 50$	Pa · s
$\lambda$	$0.045 \pm 0.006$	s
$n$	$0.33 \pm 0.03$	-
$a$	$0.85 \pm 0.04$	-

### 217 3.2. Birefringence characterization

218 Polarization imaging of the samples allows for full-field characterization of the retardance  
 219 and the principal azimuthal angle. An example of this characterization is shown in Figure 3. The  
 220 total intensity from the polarization camera array is equivalent to bright field imaging, as shown  
 221 in Figure 3a. The black horizontal line was placed on the initial layer of the printed part to  
 222 facilitate imaging - since the printed part is immersed in the refractive index matching fluid, the  
 223 multiple layers (11 in this figure) above the black line are difficult to resolve and visually similar  
 224 to the glycerol-water mixture below the horizontal line. The use of a matching fluid is necessary.  
 225 When imaged in air, the highly-curved surface of the sample causes refraction near the weld  
 226 region and obscures optical characterization in that region, see the Supplemental Information for  
 227 an example.

228 In contrast to the bright-field image, the retardance map shown in Figure 3b shows a distinct  
 229 variation in the retardance magnitude  $\rho$  across the printed part. Narrow regions of high retardance  
 230 ( $\rho \approx 65 \text{ nm}$ ) appear parallel to the printing direction and directly above regions of low retardance  
 231 ( $\rho \approx 40 \text{ nm}$ ). These regions of high and low retardance appear near the weld zone between two  
 232 extrudate layers, with the boundary between the low retardance zone and the high retardance  
 233 zone occurring approximately at the weld region. Above the high retardance region, there is an  
 234 approximate 120  $\mu\text{m}$  wide region of intermediate retardance ( $\rho \approx 50 \text{ nm}$ ) that appears near the  
 235 middle of each extrudate layer. Some streaks of higher retardance are present near the midsection  
 236 of some extrudate layers. These discontinuous horizontal streaks are defects in the printing  
 237 process that result from transient polymer build-up near the printer nozzle exit.

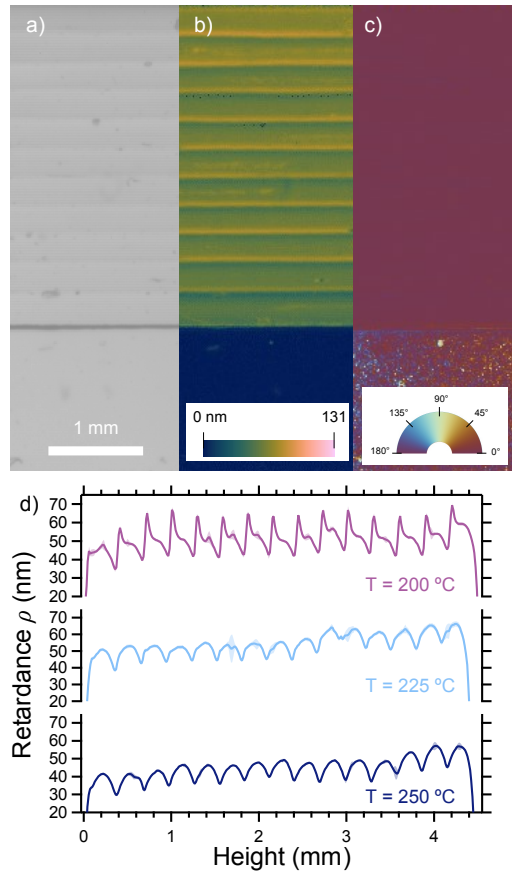


Figure 3: (a-c) Polarization imaging of a sample printed with a nozzle temperature of 200 °C and a print speed of 100 mm/s. a) Bright-field image b) Retardance image c) Principal azimuthal angle image. d) Retardance profiles of samples printed at three different temperatures. The lines indicate the average retardance over 100  $\mu\text{m}$  in the print direction, and the standard deviation of the retardance is shown via the shaded region around the average value. The corresponding Weissenberg numbers, defined in eq 4, for the prints shown in (d) are 97 ( $T = 200\text{ }^\circ\text{C}$ ), 43 ( $225\text{ }^\circ\text{C}$ ), and 24 ( $250\text{ }^\circ\text{C}$ ).

238 Although regions of constant retardance are aligned parallel to the print direction, this does  
239 not provide information on the orientation of the principal azimuthal angle  $\phi$  of the birefringence.  
240 However, polarization imaging allows for the calculation of a principal azimuthal angle map  
241 (Figure 3c). The principal azimuthal angle across the sample appears uniform, with an average  
242 magnitude of  $(0 \pm 6)^\circ$  from the print direction. This high degree of alignment occurs in all  
243 samples, independent of the nozzle temperature. For this reason, we focus the rest of this work  
244 on variations in the magnitude of the retardance and the resulting birefringence.

245 Figure 3d shows the variation in the retardance as a function of sample height, starting from  
246 the base of the first layer. The retardance at each height is the average over a  $100\ \mu\text{m}$  wide region  
247 near the center of the printed part, and the standard deviation is indicated by the shaded region.  
248 The regions of high retardance correspond to peaks in the retardance profile at  $200^\circ\text{C}$ , but at  
249 higher temperatures this feature becomes much less pronounced or is lost altogether. The parts  
250 printed at higher temperature still exhibit a periodic variation of the retardance that repeats 15  
251 times (once at each deposited layer) and closely mimics the thickness profile of the printed part.  
252 There is a systematic increase in the birefringence across the full height of the part, which can  
253 most clearly be seen when comparing the retardance in the middle of the first layer (near a height  
254 of  $0.2\ \text{mm}$ ) and the final layer (near  $4.3\ \text{mm}$ ). Samples printed with nozzle temperatures below  
255  $200^\circ\text{C}$  achieved retardances that exceed the limits of the camera, and so profiles could not be  
256 generated.

257 The measured retardance results from light propagation through birefringent parts of the  
258 sample, which may vary through the thickness. Calculations of the average chain orientation  
259 profile in material extrusion processes indicate that this is likely,[14] with the highest amount  
260 of chain orientation confined to a thin (order  $10\ \mu\text{m}$ ) layer near the polymer-air interface. The  
261 core of the extrudate layer, which would correspond to material that had exited from the center  
262 of the printer nozzle, has effectively zero orientation. Assuming that the principal azimuthal  
263 angle is constant, the retardance is an integral average of the birefringence through the thickness:  
264  $\rho = \int \Delta n(y) dy$ . We can therefore treat the measured retardance as  $\rho = w \Delta n_{avg}$ , where  $w$  is the  
265 sample thickness and  $\Delta n_{avg}$  is the average birefringence.

266 Once the sample thickness as a function of height (in the  $z$ -direction) is known, the retardance  
267 profiles from Figure 3d can be used to calculate the birefringence profiles shown in Figure 4.  
268 The parts have a constant birefringence background of  $6 \times 10^{-5}$  to  $8 \times 10^{-5}$  over the height of the  
269 printed part, which indicates that the systematic increase in retardance evident in Figure 3d is due  
270 to variations in extrudate width as a function of print height. At high printing temperatures, the  
271 birefringence profile is featureless, while at low printing temperatures there is a clear periodic  
272 peak in the birefringence that repeats at each extrudate layer. The birefringence peaks appear  
273 asymmetric in the sample printed at  $200^\circ\text{C}$ , with a skew towards greater print heights and a full  
274 width of approximately  $55\ \mu\text{m}$  at half the maximum peak birefringence. Again, birefringence  
275 profiles could not be measured for samples printed with nozzle temperatures below  $200^\circ\text{C}$ . This  
276 is due to the measurement limits of the camera.

277 These birefringence profiles can be directly mapped back onto the profiles measured from  
278 optical microscopy, as shown in Figure 5. These results demonstrate that regions of greater  
279 birefringence occur at the base of each extrudate layer and decrease gradually as one moves  
280 vertically, especially for samples printed at low nozzle temperatures. However, the birefringence  
281 is significantly decreased as one moves to the middle of an extrudate layer and is quantitatively  
282 similar to the constant birefringence observed in the samples printed at lower temperatures. Also,  
283 the birefringence profile is asymmetric across the weld zone, with the top of each extrudate  
284 layer having a significantly lower birefringence compared to the extrudate base. A similar spatial

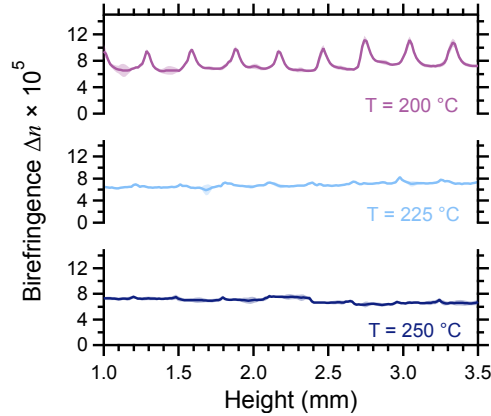


Figure 4: Birefringence profiles of samples printed at three nozzle temperatures at a print speed of 100 mm/s. The lines indicate the average across 100  $\mu\text{m}$  in the print direction, and the standard deviation is shown via the shaded region around the average value. The corresponding Weissenberg numbers for these prints are the same as in Fig. 3.

285 variation is present in the part printed at 225  $^{\circ}\text{C}$ , although much less pronounced than at lower  
 286 printing temperatures. It is important to note that the regions of highest birefringence also occur  
 287 where the sample has the highest curvature and are only visible when imaging the sample in an  
 288 index matching fluid.

289 Although the birefringence profile suggests that there is a higher degree of chain orientation  
 290 at the base of each extrudate layer, mysteries remain: what is the origin of the constant birefringence  
 291 that occurs at higher printing temperatures? One possible explanation is that the extrudate  
 292 is uniformly drawn during extrusion and deposition, which would result from a velocity mis-  
 293 match between the print head translation velocity and the average velocity of the molten polymer  
 294 extruded from the nozzle. This extensional deformation would uniformly orient chains in the  
 295 print direction throughout the extrudate and would be superimposed with the deformation of the  
 296 extrusion-deposition process. Significant chain stretching is also expected during the deposition  
 297 process as a result of 90 $^{\circ}$  turn in the extrusion path between the printer nozzle and the printed  
 298 layer.[7] However, chain stretch relaxes at the Rouse timescale, which is much faster than the  
 299 reptation timescale governing orientation relaxation. Prior work has shown that any chain stretch  
 300 imparted from the extrusion-deposition process relaxes to negligible magnitudes as the extrudate  
 301 cools.[16]

302 A second possible explanation is the buildup of residual thermal stresses in the part that  
 303 occurs as the sample cools below the glass transition temperature. This is a common phenomenon  
 304 in material extrusion that often manifests by dimensional warping in the final part.[38] These  
 305 residual stresses can be measured using a variety of destructive techniques,[39] but for optically  
 306 transparent materials the residual thermal stress results in birefringence.[22] The relationship  
 307 between residual stress and birefringence is governed a linear stress optic rule,  $\mathbf{n} = C_{\text{RS}}\boldsymbol{\sigma}$ , where  
 308 the stress-optic coefficient due to residual stress  $C_{\text{RS}}$  can be different in magnitude and sign from  
 309 the coefficient due to trapped chain orientation  $C_{\text{OR}}$ .[40]

310 Since residual thermal stresses occur from nonuniform cooling below the glass transition  
 311 temperature, annealing the samples at temperatures slightly above the glass transition temper-  
 312 ature of PLA should remove these thermal stresses while leaving the residual orientation un-

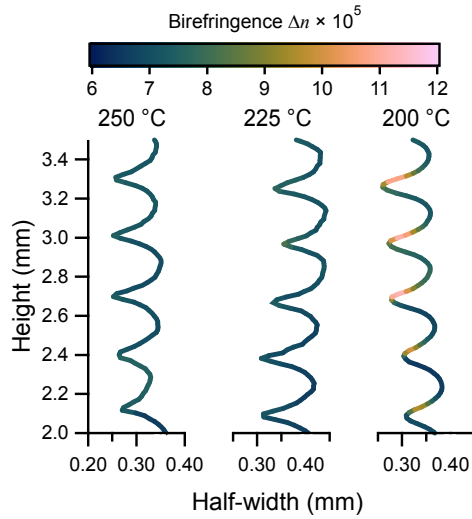


Figure 5: Birefringence profiles mapped onto the profiles of the parts printed at 100 mm/s and the indicated nozzle temperatures. The corresponding Weissenberg numbers for these prints are the same as in Fig. 3.

313 changed. To test this concept, we anneal the samples for 3 min at a temperature of 65 °C. Po-  
 314 larized optical images of this process are shown in Figure 6. Birefringence in the bulk of each  
 315 extrudate layer is dramatically reduced to negligible levels within approximately 30 s after the  
 316 sample has reached the annealing temperature, while birefringence near the weld region remains.  
 317 The rapid loss of birefringence indicates that much of the residual stresses in these parts are from  
 318 thermal stresses. Since these stresses are generated in the glassy state, the birefringence origi-  
 319 nates from molecular-scale (bond length or angle)[41] deformations which can relax at very  
 320 fast timescales above the glass transition temperature. Holding the sample at 65 °C for extended  
 321 durations does not reduce the birefringence observed near the weld, which indicates that both  
 322 chain relaxation and crystallization processes are sufficiently slow at this temperature to have  
 323 no effect on the residual orientation templated into the sample from the printing process. Chain  
 324 relaxation timescales can be estimated from our rheology measurements: extrapolating the relax-  
 325 ation timescales to our annealing temperature, we estimate the Rouse (chain stretch) relaxation  
 326 timescale to be on the order of  $10^3$  s, which is an order of magnitude longer than our annealing  
 327 time. We note that annealing PLA samples at higher temperatures for prolonged periods of time  
 328 is an established technique to increase mechanical strength in parts.[29, 42, 43]

329 Birefringence profiles of annealed samples are shown in Fig 7a. After annealing, the mea-  
 330 sured birefringence magnitude is much lower than the pre-annealed samples (Fig 4). This is  
 331 especially true for the samples that were printed at 225 °C and 250 °C which, after annealing,  
 332 have birefringence values of approximately  $10^{-5}$  or less. This is further evidence that the ap-  
 333 proximately constant birefringence background observed for non-annealed samples printed at  
 334 these conditions is due solely to residual thermal stresses.

335 The birefringence profile of the sample printed at 200 °C and 100 mm/s exhibits a clear pe-  
 336 riodicity that consists of a narrow region of high birefringence followed by a broader region  
 337 of smaller (though non-negligible) birefringence. The narrow region of strong birefringence  
 338 appears as a peak with a maximum near  $6 \times 10^{-5}$  and approximate width of 50  $\mu\text{m}$  to 60  $\mu\text{m}$

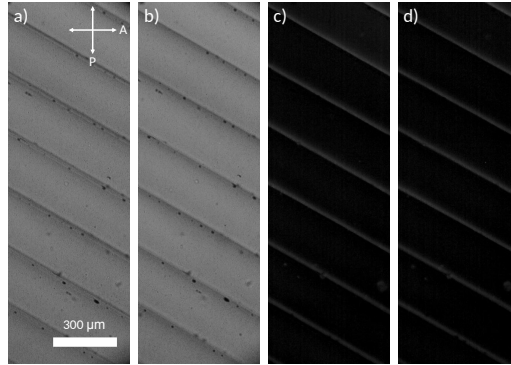


Figure 6: Polarized optical images of the sample printed at a nozzle temperature of 225 °C during the heating step to remove thermal stresses: a) 22 °C, prior to heating, b) 65 °C for 5 s, c) 65 °C for 35 s, d) 65 °C for 250 s.

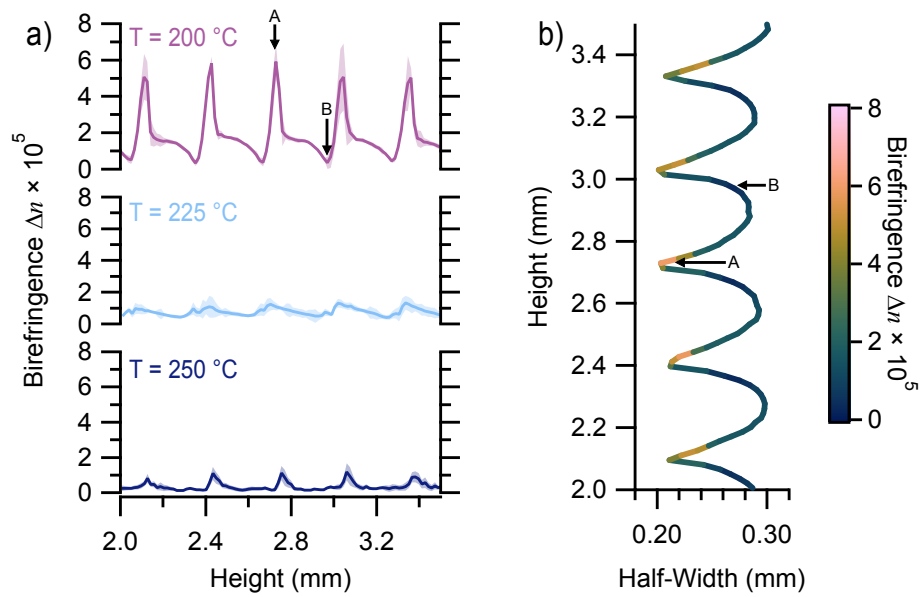


Figure 7: a) Birefringence profiles of annealed samples printed at the same conditions as Fig 4. The lines indicate the average calculated value across 100 μm in the print direction, and the standard deviation is shown via the shaded region around the average value. b) Birefringence mapped onto the profile of the part printed at 200 °C and 100 mm/s. Arrows indicate the position of maximum birefringence (“A”) and minimum birefringence (“B”) in a single extrudate layer. The corresponding Weissenberg numbers for these prints are the same as in Fig. 3.

339 (indicated by “A” for a single layer in Fig 7). By mapping the birefringence intensity back to the  
 340 profile of the printed part as shown in Fig 7b, we see that this strong birefringence still appears  
 341 near the bottom of each extrudate layer and very close to the weld zone. An additional region of  
 342 broad birefringence of approximately  $2 \times 10^{-5}$  appears in this annealed sample, indicating that  
 343 residual orientation persists further away from the weld region. Close inspection of the birefrin-  
 344 gence mapped to the printed profile indicates that this region of lower birefringence decreases  
 345 rapidly above the mid-height of each extrudate layer (indicated by “B” for a single layer in Fig  
 346 7). Birefringence imaging of annealed samples printed at lower temperatures was not possible  
 347 because the retardance near the weld region exceeded the range of the camera.

348 The annealed birefringence profiles indicate a strong temperature dependence on not only  
 349 the magnitude of the residual orientation, but also the spatial variation of orientation within an  
 350 extrudate layer. Although a complete numerical simulation of the extrusion-deposition process is  
 351 beyond the scope of this manuscript, the variation in birefringence as a function of height agrees  
 352 qualitatively with the simulation results of Costanzo *et al.* for polylactide material extrusion.[14]  
 353 In their work, they calculated the residual orientation profile in the cross-section of an extrudate  
 354 layer for fast and slow printing conditions at a constant nozzle temperature.

355 We can compare our results with prior work by using the dimensionless ratio of the timescale  
 356 governing polymer relaxation and a characteristic process timescale. This ratio is called the  
 357 Weissenberg number,  $Wi$ . Here, we choose the reptation time of the polymer at the nozzle  
 358 temperature  $\tau_d(T)$  as the timescale for polymer relaxation, since deformation rates faster than  
 359  $\tau_d^{-1}$  result in chain orientation in flow. The characteristic process timescale that we will choose is  
 360 the inverse of the shear rate at the wall of the printer nozzle  $\dot{\gamma}_w$ . We will assume fully-developed  
 361 nozzle flow of a power-law fluid, [8]

$$\dot{\gamma}_w = \frac{4Q}{\pi R^3} \frac{3n+1}{4n}, \quad (3)$$

362 where  $R$  is the nozzle radius and  $n$  is the power-law index. The volumetric flow rate in the nozzle  
 363  $Q$  is calculated from the initial filament cross-section ( $6.5 \text{ mm}^2$ ) and the print velocity. Based  
 364 on the variation in the filament diameter, we expect a relative uncertainty in the volumetric flow  
 365 rate of 4%. For the print speeds used here, the wall shear rate falls in the approximate range of  
 366 (200 to 2000)  $s^{-1}$ , which is well within the shear-thinning range (see Fig. 2b). The Weissenberg  
 367 number is then

$$Wi = \tau_d(T)\dot{\gamma}_w \quad (4)$$

368 which is referred to as “the local Weissenberg number at the nozzle wall” in the work of McIlroy  
 369 and Olmsted.[7]

370 Higher  $Wi$  corresponds to process flows that orient the polymer chains more strongly. Note  
 371 that there are two ways to increase  $Wi$ : either 1) increase the wall shear rate (increase print speed)  
 372 at a fixed reptation timescale (fixed temperature), or 2) increase the reptation timescale (*decrease*  
 373 temperature) at a fixed wall shear rate (fixed print speed). From this, we can generate a schematic  
 374 diagram of the orientation in the cross-section of an extrudate layer as shown in Figure 8 based  
 375 on the results of Costanzo *et al.*[14] for high and low nozzle  $Wi$ . Although a direct comparison  
 376 is not possible because they did not determine a shear thinning exponent to estimate wall shear  
 377 rates in the nozzle, Costanzo *et al.* do provide enough information to calculate a “mass-averaged  
 378 Weissenberg number”, [7] defined as  $\overline{Wi} = \tau_d(T)U_N/R$  where  $U_N$  is the print speed and  $R$  is  
 379 the nozzle radius. The mass-averaged Weissenberg number will always be roughly an order of  
 380 magnitude less than  $Wi$  as defined in eq 4, and  $\overline{Wi}$  neglects the higher shear rate (and greater

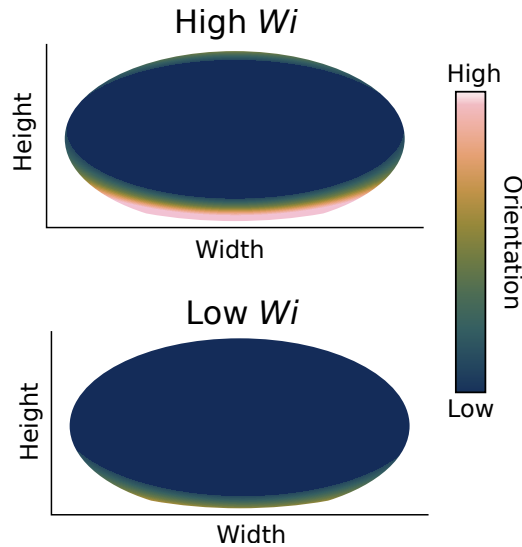


Figure 8: Schematic diagram of the expected residual orientation in the cross-section of an annealed extrudate layer based on the results of Costanzo *et al.*[14] based on the  $Wi$  of the molten polymer in the printer nozzle. Here, “Low  $Wi$ ” corresponds to  $Wi \sim 10$  and “High  $Wi$ ” corresponds to  $Wi \sim 100$ .

381 degree of chain orientation) near the nozzle wall expected for shear-thinning polymer melts. For  
 382 Costanzo *et al.*  $R = 0.2$  mm, the print speeds  $U_N$  used in calculating the residual orientation  
 383 profiles are 20 mm/s and 120 mm/s, and based on their rheology measurements the reptation  
 384 time for their polylactide at the printing temperature is  $\tau_d(180^\circ\text{C}) = 0.029$  s.[14] From this, we  
 385 estimate that the conditions corresponding to “Low  $Wi$ ” occur for  $Wi \sim 10$  and “High  $Wi$ ” occur  
 386 for  $Wi \sim 100$  in Figure 8.

387 As shown in Figure 8, residual chain orientation remains trapped in a boundary layer near the  
 388 lower part of each extrudate cross-section, which is also the section of extrudate that is highly  
 389 deformed during the deposition process. Conditions where  $Wi \sim 10$  result in a lower magnitude  
 390 of chain orientation. Printing conditions where  $Wi \sim 100$  result in both an increase in the  
 391 magnitude of residual orientation near the weld region, as well as a nonzero amount of orientation  
 392 near the top of the extrudate cross-section. Even at higher  $Wi$ , the center of each extrudate layer  
 393 retains negligible chain orientation. These predictions match well with our experimental results,  
 394 where the region of zero birefringence (and negligible chain orientation) occurs above the mid-  
 395 plane of the extrudate layer. Our results in Figure 7b, where  $Wi = 97$ , also show nonzero residual  
 396 orientation near the top of each extrudate layer in agreement with the  $Wi \sim 100$  schematic  
 397 diagram.

### 398 3.3. Process dependence of near-weld residual orientation

399 Since chain orientation at weld is thought to play a role in weld strength and overall mechan-  
 400 ical properties in printed parts, it is important to understand how processing conditions affect  
 401 the near-weld orientation via birefringence. By measuring the retardance at the weld and the  
 402 weld thickness, we can calculate the resulting birefringence due to chain orientation as a function  
 403 of the print parameters as shown in Figure 9. Higher birefringence occurs near the weld when  
 404 samples are printed at lower temperatures and faster print speeds. We can estimate the degree

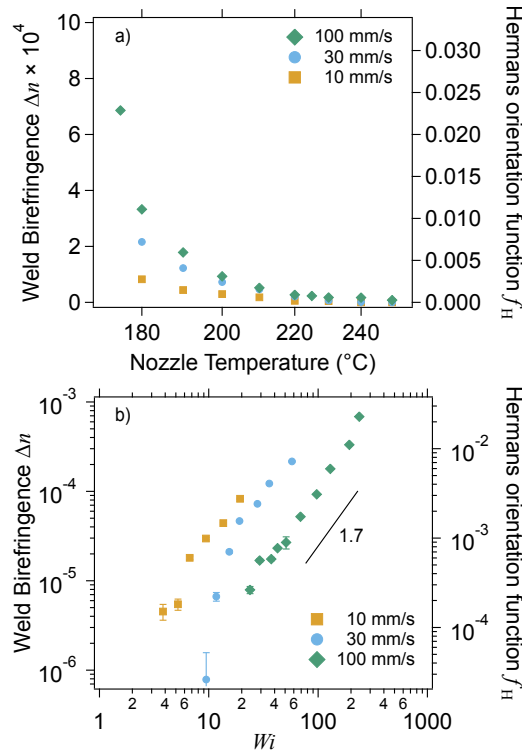


Figure 9: a) Weld birefringence and chain orientation as a function of nozzle temperature and print speed. b) The same results as in (a) as a function of  $Wi$ . Error bars represent measurement uncertainty from the propagated error from uncertainty in the retardance and width measurements.

405 of chain alignment by comparing the measured birefringence  $\Delta n$  with the intrinsic birefringence  
 406 of an ordered PLA chain,  $\Delta n_0 = 0.03$ .<sup>[44]</sup> Although this  $\Delta n_0$  was calculated for a crystal unit  
 407 cell of PLA, mechano-optical measurements of amorphous PLA films under uniaxial deforma-  
 408 tion approach this birefringence value at large strain.<sup>[28]</sup> The ratio  $\Delta n/\Delta n_0$  is equal to Hermans  
 409 orientation function  $f_H$ : a value of 0 corresponds to a randomly-oriented (equilibrium) configura-  
 410 tion, while a value of 1 corresponds to all chains oriented in the same direction, which in  
 411 this case is parallel to the printing direction. Higher magnitudes of birefringence occur at lower  
 412 printing temperatures and faster printing speeds, which agrees with the current understanding of  
 413 the printing process: at higher print speeds there is increased chain deformation as a result of the  
 414 extrusion and deposition process. Lower print temperatures have a compounding effect, since the  
 415 polymer chains will relax more slowly at lower temperatures and the extrudate takes less time to  
 416 cool below the glass transition temperature, resulting in increased trapped chain orientation.

417 Despite the strong dependence of this trapped orientation on printing conditions, the overall  
 418 magnitude of the chain orientation near the weld is small - approximately 2 % according to  $f_H$ .  
 419 This small amount of trapped orientation results from the competition between relaxation and  
 420 cooling in the as-deposited extrudate. Although we do not directly calculate it here, results from  
 421 prior continuum modeling efforts suggest that the residual chain orientation is approximately  
 422 an order of magnitude less than the as-deposited orientation.<sup>[7, 14]</sup> Parts printed at the highest

423 temperature and print speed did not retain any resolvable residual chain orientation.

424 The weld birefringence is shown as a function of  $Wi$  in Figure 9b. Here, there is a systematic  
425 increase in weld birefringence with  $Wi$  at a constant print speed, but for a fixed  $Wi$ , printing  
426 at slower nozzle speeds generates significantly more chain orientation near the weld region. If  
427 nozzle flow were the sole contributor to residual chain orientation, then we would expect data to  
428 collapse onto a single curve regardless of print speed. However, measurements at one print speed  
429 appear horizontally shifted from measurements at a different print speed. This deviation reflects  
430 the physics not incorporated in the scaling analysis, which includes 1) die swell that occurs as the  
431 polymer exits the nozzle,[45] 2) additional chain deformation from the deposition and spreading  
432 process, and 3) orientation relaxation that occurs after deposition while the polymer cools. Faster  
433 printing speeds can also result a lower temperature at the core of the extrudate compared to the  
434 part of the extrudate that was in contact with the nozzle wall, resulting in core temperatures that  
435 can be up to 30 °C cooler than the nozzle temperature.[46] Although this is not incorporated in  
436 the scaling analysis, we note that the weld birefringence as a function of  $Wi$  shown in Figure 9b  
437 does not show a strong variation in slope as printing speed increases. We therefore expect the  
438 temperature profile in the extrudate to have a minor contribution to the residual birefringence.

439 Despite this missing physics, all three printing speeds exhibit an approximate power law  
440 dependence of  $\Delta n \sim Wi^{1.7}$ . Deviations from this power law occur at the lowest  $Wi$  for each  
441 print speed. Since low  $Wi$  corresponds with higher nozzle temperatures, the lower weld birefrin-  
442 gence observed at higher nozzle temperatures indicates that the oriented polymer chains from the  
443 extrusion-deposition process have had more time to relax before becoming trapped at  $T_g$ . This  
444 agrees qualitatively with prior simulation results of orientation relaxation during cooling.[14]  
445 The relatively strong  $Wi^{1.7}$  power law dependence can be compared to the scaling of the orienta-  
446 tion based on fully developed capillary flow, which we estimate as follows: the chain orientation  
447 near the wall should depend on the shear stress and the first normal stress difference according to  
448 the principal stress difference[34]

$$\Delta\sigma = \sqrt{4\tau_{rz}^2 + N_1^2} \quad (5)$$

449 where  $\tau_{rz}$  is the shear stress at the wall and  $N_1 = \tau_{rr} - \tau_{zz}$  is the first normal stress difference. We  
450 can estimate the first normal stress difference from the oscillatory rheology data using Laun's rule  
451 (see Supplemental Information)[47] and substitute both shear stress and first normal stress differ-  
452 ence into eq 5, the resulting scaling for the stress (and via the stress optic law, the birefringence)  
453 in the high shear-rate range is  $\Delta\sigma \sim Wi^{0.62}$ .

454 The disagreement between the measured scaling and the expected scaling from capillary  
455 flow indicates that a complete description of the residual orientation cannot be explained solely  
456 by flow in the printer nozzle. Although McIlroy and Olmsted developed a kinematic description  
457 of polymer chain deformation as the polymer makes the 90° turn during deposition,[7] the model  
458 does not include an effect of deposition *rate* on the resulting residual chain orientation. More  
459 recent computational fluid dynamics efforts have shown that the flow field and deformation re-  
460 sulting from the deformation process will require more than a kinematic approximation.[48, 49]  
461 A full simulation of the extrusion-deposition process that includes viscoelastic effects is beyond  
462 the scope of this manuscript.

463 Despite these challenges, we have demonstrated that the residual chain orientation can be  
464 approximated by a simple power law dependence on  $Wi$  based on flow in the nozzle. Thus,  
465 residual chain orientation can be printed into parts in a controlled manner.

#### 466 4. Conclusions

467 Birefringence in parts printed in material extrusion processes has two separate origins. The  
468 first contribution to the birefringence comes from residual chain orientation from the extrusion-  
469 deposition process that does not have time to relax to equilibrium before the sample cools below  
470 the glass transition temperature. The second contribution to birefringence comes from a residual  
471 stress build-up as the part cools non-uniformly below the glass transition. In order to mea-  
472 sure and characterize residual chain orientation, the residual stress must be removed. Here, we  
473 demonstrate that uniform annealing of the sample slightly above the glass transition tempera-  
474 ture removes the residual stress without significantly affecting residual chain orientation. This  
475 residual orientation is orientated in the printing direction and occurs near the weld region at the  
476 base of each extrudate layer. The weld birefringence has a strong power-law dependence on the  
477 Weissenberg number (based on nozzle flow) across different print speeds, but the lack of overlap  
478 in the data indicates that the deposition process has a strong contribution to the resulting chain  
479 orientation. The power-law relationship developed here demonstrates that residual orientation  
480 can be readily tuned via process parameters like print speed and nozzle temperature when com-  
481 bined with characterization of polymer relaxation timescales from rheology. Immediate future  
482 work involves the direct measurement of weld mechanical properties for samples printed with  
483 similar magnitudes of chain orientation but different  $Wi$  to isolate the effects of residual orien-  
484 tation on weld strength and fracture toughness. Our results motivate additional theoretical and  
485 modeling efforts to describe this relationship and provide a critical test for previously developed  
486 computational fluid dynamics efforts to simulate the polymer material extrusion process.

487 The ability to quantify residual orientation near the weld is critical to testing models relating  
488 molecular morphology to weld strength, and this work motivates efforts to isolate and charac-  
489 terize the different contributions to overall part strength. Although not the focus of this work,  
490 we have shown that residual thermal stresses will occur in material extrusion processes. Future  
491 directions for this work are the quantification and spatial variation in residual thermal stresses in  
492 more complicated geometries and print paths, as well as the effect of this residual stress on me-  
493 chanical part properties separate from residual orientation to accelerate novel printing strategies  
494 to tune part properties.

#### References

- [1] K. Rajan, M. Samykano, K. Kadirgama, W. S. W. Harun, M. M. Rahman, *The International Journal of Advanced Manufacturing Technology* **2022**, *120*, 1531–1570.
- [2] N. Betancourt, X. Chen, *Bioprinting* **2022**, *25*, e00189.
- [3] K. R. Ryan, M. P. Down, C. E. Banks, *Chemical Engineering Journal* **2021**, *403*, 126162.
- [4] Z. Tadmor, *Journal of Applied Polymer Science* **1974**, *18*, 1753–1772.
- [5] J. E. Seppala, K. D. Migler, *Additive Manufacturing* **2016**, *12*, 71–76.
- [6] A. Das, C. McIlroy, M. J. Bortner, *Progress in Additive Manufacturing* **2021**, *6*, 3–17.
- [7] C. McIlroy, P. D. Olmsted, *Journal of Rheology* **2017**, *61*, 379–397.
- [8] C. W. Macosko, *Rheology: principles, measurements, and applications*, Wiley-vch, **1994**.
- [9] B. G. Compton, J. A. Lewis, *Advanced Materials* **2014**, *26*, 5930–5935.
- [10] S. Gantenbein, K. Masania, W. Woigk, J. P. W. Sesseg, T. A. Tervoort, A. R. Studart, *Nature* **2018**, *561*, 226–230.
- [11] A. Rodriguez-Palomo, V. Lutz-Bueno, M. Guizar-Sicairos, R. Kádár, M. Andersson, M. Liebi, *Additive Manufacturing* **2021**, *47*, 102289.

- [12] D. M. Roper, K.-A. Kwon, L. P. Malone, S. M. Best, R. E. Cameron, *Advanced Materials Technologies* **2022**, 2200139.
- [13] M. A. G. Cunha, M. O. Robbins, *Macromolecules* **2020**, *53*, 8417–8427.
- [14] A. Costanzo, R. Spotorno, M. V. Candal, M. M. Fernández, A. J. Müller, R. S. Graham, D. Cavallo, C. McIlroy, *Additive Manufacturing* **2020**, *36*, 101415.
- [15] A. Costanzo, A. Poggi, S. Looijmans, D. Venkatraman, D. Sawyer, L. Puskar, C. McIlroy, D. Cavallo, *Polymers* **2022**, *14*, 2792.
- [16] C. McIlroy, J. E. Seppala, A. P. Kotula in *Polymer-Based Additive Manufacturing: Recent Developments*, ACS Symposium Series, American Chemical Society, **2019**, Chapter 6, pp. 85–113.
- [17] D. W. Collinson, N. Von Windheim, K. Gall, L. C. Brinson, *Additive Manufacturing* **2022**, *51*, 102604.
- [18] N. M. Hassan, K. B. Migler, A. R. Hight Walker, A. P. Kotula, J. E. Seppala, *MRS Communications* **2021**, *11*, 157–167.
- [19] Y. Shmueli, Y.-C. Lin, S. Lee, M. Zhernenkov, R. Tannenbaum, G. Marom, M. H. Rafailovich, *ACS Applied Materials & Interfaces* **2019**, *11*, 37112–37120.
- [20] A. Adhikari, T. Bourgade, A. Asundi, *Theoretical and Applied Mechanics Letters* **2016**, *6*, 152–156.
- [21] J. C. Seferis, *The Wiley Database of Polymer Properties* **2003**.
- [22] R. Wimberger-Friedl, *Progress in Polymer Science* **1995**, *20*, 369–401.
- [23] L. C. E. Struik, *Polymer Engineering Science* **1978**, *18*, 799–811.
- [24] P. So, L. J. Broutman, *Polymer Engineering Science* **1976**, *16*, 785–791.
- [25] A. Siegmund, A. Buchman, S. Kenig, *Polymer Engineering Science* **1981**, *21*, 997–1002.
- [26] M. Van Gurp, J. Palmén, *Rheol. Bull* **1998**, *67*, 5–8.
- [27] T. Onuma, Y. Otani, *Optics Communications* **2014**, *315*, 69–73.
- [28] J. Mulligan, M. Cakmak, *Macromolecules* **2005**, *38*, 2333–2344.
- [29] W. Yu, X. Wang, X. Yin, E. Ferraris, J. Zhang, *Materials & Design* **2023**, *226*, 111687.
- [30] A. E. Likhtman, T. C. B. McLeish, *Macromolecules* **2002**, *35*, 6332–6343.
- [31] V. A. H. Boudara, D. J. Read, J. Ramírez, *Journal of Rheology* **2020**, *64*, 709–722.
- [32] T. C. B. McLeish, *Advances in Physics* **2002**, *51*, 1379–1527.
- [33] H. Janeschitz-Kriegl, *Polymer melt rheology and flow birefringence*, Vol. 6, Springer Science & Business Media, **2012**.
- [34] G. G. Fuller, *Optical rheometry of complex fluids*, Oxford University Press, **1995**.
- [35] M. L. Williams, R. F. Landel, J. D. Ferry, *Journal of the American Chemical Society* **1955**, *77*, 3701–3707.
- [36] W. P. Cox, E. H. Merz, *Journal of Polymer Science* **1958**, *28*, 619–622.
- [37] K. Yasuda, R. C. Armstrong, R. E. Cohen, *Rheologica Acta* **1981**, *20*, 163–178.
- [38] M. Mahesh, Y. S. Wong, J. Y. H. Fuh, H. T. Loh, *Rapid Prototyping Journal* **2004**, *10*, 123–135.
- [39] A. Turnbull, A. S. Maxwell, S. Pillai, *Journal of Materials Science* **1999**, *34*, 451–459.
- [40] K. Osaki, H. Okamoto, T. Inoue, E.-J. Hwang, *Macromolecules* **1995**, *28*, 3625–3630.
- [41] T. Inoue, H. Matsui, S. Murakami, S. Kohjiya, K. Osaki, *Polymer* **1997**, *38*, 1215–1220.
- [42] I. A. Reis, P. I. Cunha Claro, A. L. Marcomini, L. H. Capparelli Mattoso, S. P. da Silva, A. R. de Sena Neto, *Polymer Engineering & Science* **2021**, *61*, 2097–2104.
- [43] S. Wang, L. Daelemans, R. Fiorio, M. Gou, D. R. D’hooge, K. De Clerck, L. Cardon, *Polymers* **2019**, *11*, DOI 10.3390/polym11091529.
- [44] Y. Furuhashi, Y. Kimura, H. Yamane, *Journal of Polymer Science Part B: Polymer Physics* **2007**, *45*, 218–228.
- [45] A. R. Colon, D. O. Kazmer, A. M. Peterson, J. E. Seppala, *Additive Manufacturing* **2023**, *73*, 103700.
- [46] C. Luo, X. Wang, K. B. Migler, J. E. Seppala, *Additive Manufacturing* **2020**, *35*, 101361.
- [47] H. M. Laun, *Journal of Rheology* **1986**, *30*, 459–501.
- [48] S. K. Kim, D. O. Kazmer, *Additive Manufacturing* **2022**, *55*, 102833.
- [49] H. Zhang, F. Ye, F. Chen, W. Yuan, W. Yan, *Additive Manufacturing* **2024**, *81*, 103992.